JOURNAL OF SYNCHROTRON RADIATION

ISSN 1600-5775

Received 11 June 2020
Accepted 5 November 2020

Edited by M. Wang, Paul Scherrer Institute, Switzerland

Keywords: X-ray tomography; temporal resolution; high-speed rotation.

Supporting information: this article has supporting information at journals.iucr.org/s

High-speed rotating device for X-ray tomography with 10 ms temporal resolution

Ryo Mashita,[a] Wataru Yashiro,[b]* Daisuke Kaneko,[c] Yasumasa Bito[a] and Hiroyuki Kishimoto[a]

[a]Sumitomo Rubber Industries Ltd, Kobe, Hyogo 651-0071, Japan, [b]Institute of Multidisciplinary Research for Advanced Materials (IMRAM), Tohoku University, Japan, and [c]SAITO Machine Industry Co. Ltd, Japan. *Correspondence e-mail: wyashiro@tohoku.ac.jp

The temporal resolution of X-ray tomography, using a synchrotron radiation X-ray source, has been improved to millisecond order in recent years. However, the sample must be rotated at a speed of more than a few thousand revolutions per minute, which makes it difficult to control the environment around the sample. In this study, a high-speed rotation device has been developed, comprising two synchronized coaxial motors movable along the direction of the axis, which can stretch or compress the rotating sample. Using this device, tomograms of breaking rubber were successfully obtained at a temporal resolution of 10 ms.

1. Introduction

The demand for visualizing internal structures with high temporal and spatial resolutions is increasing in various fields such as materials and life sciences. High-speed X-ray tomography can provide a solution for such demand. There is generally a trade off between temporal and spatial resolutions. Therefore, the improvement in sensitivity and the use of a high-flux X-ray beam are required for a high temporal resolution without sacrificing the spatial resolution.

In previous studies, millisecond-order X-ray phase tomography for a rotating sample was successfully realized using X-ray phase-contrast imaging techniques (Yashiro *et al.*, 2017*a*,*b*, 2018*a*; García-Moreno *et al.*, 2019). The use of a fringe-scanning method (Bruning *et al.*, 1974; Schreiber & Bruning, 2007; Hack & Burke, 2011) enabled spatial and temporal resolutions of 20 µm and 4.43 ms to be achieved, respectively, using a bending-magnet beamline at SPring-8, Japan (Yashiro *et al.*, 2018*b*). Although rotating the sample alone at high speed is comparatively easy, rotating the sample along with environmental change such as compressive or tensile deformation at high speed is not easy with respect to the rotational stability and synchronization.

In this study, we present a high-speed rotation device for four-dimensional computed tomography (4D-CT) with a temporal resolution of 10 ms consisting of two synchronized coaxial motors movable along the direction of the axis, which can stretch or compress the rotating sample. In Section 2, we describe the design of the device and the experimental setup for high-speed X-ray tomography. In Section 3, we demonstrate the X-ray tomography of breaking rubber with a temporal resolution of 10 ms. In Section 4, we discuss the benefits and unique capability of our equipment as well as its intended application in future work.

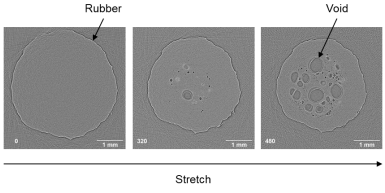

2. Design of the rotating device and experimental setup for X-ray tomography

Fig. 1(*a*) shows a schematic illustration of the rotating device for high-speed X-ray tomography developed with Touhoku Sokki Corp. It comprises two coaxial inverter-driven motors [Mitsubishi Electric Corporation, horizontal-type SF-JR (200 V-2P-0.2 kW)], which can be electrically synchronized by the motor controller WJ200 (Hitachi Industrial Equipment Systems Co. Ltd). It is possible to maintain a degree of wobble of the two rotation axes within ±2 µm. This value is smaller than the camera pixel size of 5 µm, suggesting that the wobble of the two rotation axes has negligible effect on the data quality. The motors for rotation are mounted on two carriages on parallel stainless-steel rails with lead screws and are uniaxially movable along the rails in a direction parallel to the rotation axis. The motor and motor controller used for linear motion are the BLM230-GFV2 and BMUD30-A2 (Oriental motor Co. Ltd), respectively. Thereby, a sample bonded on top of the motor axes (brass rods) can be stretched or compressed at high-speed rotation. The compressive and tensile displacement speeds of our device range from 42.0 to 3358.3 µm s^{-1} without load, and, even with load, they can be experimentally determined from the distance between the edges of both brass rods. The rotation speed can range from 6 to 12 000 rpm. The rotation accuracy of the motor used in our device is ±0.01%, suggesting that the motor rotational fluctuation has negligible effect on the CT reconstruction images. If necessary, the axes can be connected using two pieces of copper wire, the centrifugal force acting on which aids the synchronization of motor rotation. In the case of a relatively rigid sample (*e.g.* rubber) motor rotation can be kept synchronized without using the wires. The axial thrust load capacity of the motors is 175 N, which was sufficiently high to stretch and break the rubber sample. Figs. 1(*b*) and 1(*c*) show photographs of the rotating device [(*b*) without and (*c*) with a rubber sample].

Fig. 2 shows the experimental setup for high-speed CT using the developed rotating device. The CT experiment was performed using BL28B2 at SPring-8, Japan, where a white synchrotron X-ray beam from a bending-magnet source was available. An X-ray image detector, comprising a scintillator screen, lenses and high-speed CMOS camera (Photron FASTCAM NOVA S12), was used to obtain the X-ray projection images. For the scintillator screen, we used a 10 µm-thick GAGG single-crystal (Ce: $Gd_3Al_2Ga_3O_{12}$) plate, which has an excellent scintillation light yield and a short decay time of 53 ns (Kamada *et al.*, 2011). The full width at half-maximum of the point spread function was 5 µm.

3. Demonstration of high-speed X-ray tomography

We performed high-speed CT with a temporal resolution of 10 ms for breakage of rubber used for tires, the vulcanizate of which comprises styrene-butadiene rubber (SBR), silica particles, sulfur and a vulcanization accelerator. The rubber sample was cylindrical with 4 mm diameter and 0.5 mm height. The sample was attached to the brass rods with glue [see Fig. 1(*c*)]. The breakage phenomenon of rubber has not yet been completely elucidated because of the complexity of

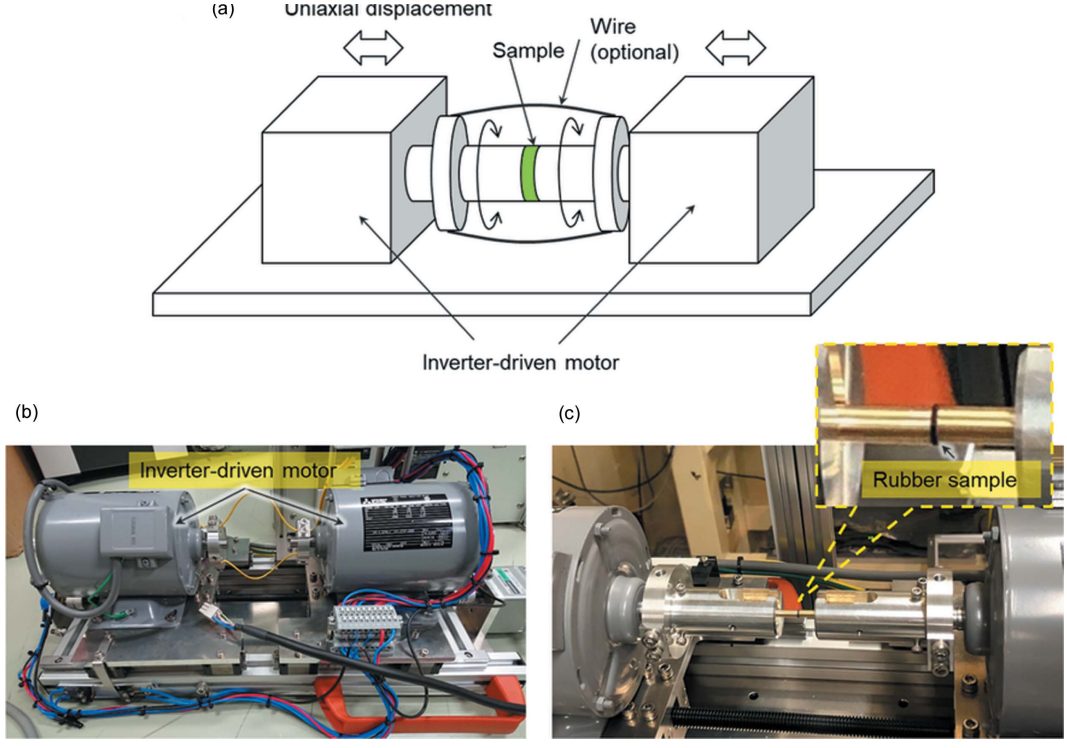

Figure 1
(*a*) Schematic illustration of the rotating device for high-speed X-ray tomography, and (*b*, *c*) photographs of the rotating device developed [(*b*) without and (*c*) with the sample, respectively].

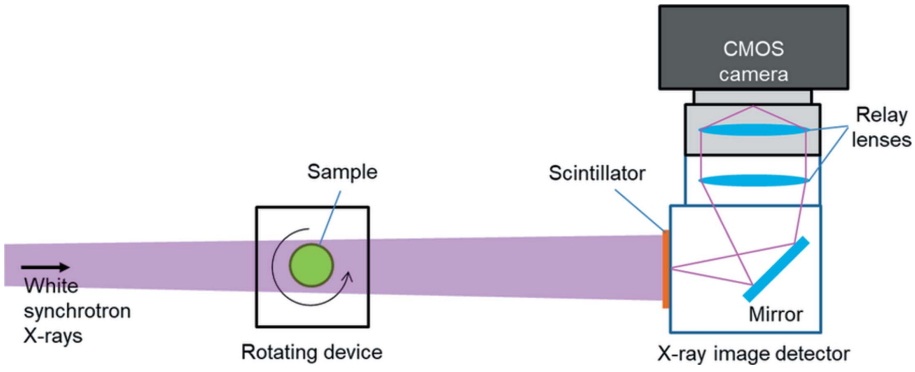

Figure 2
Experimental setup for X-ray tomography using the rotating device (side view).

rubber material, which includes various added agents. X-ray CT observation with high temporal resolution as presented in this study is necessary for understanding the breakage phenomenon of rubber and improving the fracture resistance property of tire rubber.

The experimental conditions are as follows: sample rotation speed: 3000 rpm; sample-to-image detector distance: 4.7 m; frame rate: 12 800 frames s^{-1}; field of view: 1024 × 1024 pixels; effective pixel size at the sample position: 4.5 µm; exposure time: 78.125 µs (1/12800 s); and number of projections for half-turn of the sample: 128. A 15 mm-thick aluminium plate was placed on the upper-stream side of the camera as an X-ray absorber.

Fig. 3(*a*) shows examples of the X-ray projection images [propagation-based phase-contrast images (Snigirev *et al.*, 1995; Wilkins *et al.*, 1996; Cloetens *et al.*, 1996; Socha *et al.*, 2007; Lee *et al.*, 2011)] obtained from the sample. The number in the bottom-left corner is the time in milliseconds from the beginning of stretching. From such projection images, it was confirmed that the sample was stretched at a constant rate of 1226.8 µm s^{-1}. Fig. 3(*b*) and Movie S1 of the supporting information show the time-resolved tomograms of stretching rubber with a temporal resolution of 10 ms (in the middle of the top of the two rods). Each scan was performed after 180° rotation of the sample, obtained by applying a standard filtered-back projection algorithm to the minus logarithm of transmittance images. Although a projection number of 128 is considered low, the formation and growth process of voids within the rubber were qualitatively viewed in the CT reconstructed images. Note that a compressed sensing algorithm using total variation regularization (Yashiro *et al.*, 2017*a*,*b*; Li *et al.*, 2002; Donoho, 2006; Sidky & Pan, 2008; Defrise *et al.*, 2011; Kudo *et al.*, 2016; Wang *et al.*, 2019) can be used for obtaining high single-to-noise ratio CT reconstruction images with a low projection number. The discontinuities at the fringes around some of the developing voids in the sample, observed in both Fig. 3(*b*) and Movie S1, are motion artifacts, indicating that the growth speed of the void is more than the temporal resolution of 10 ms. The contrast of the obtained tomograms was not quantitative because the projection images include propagation-based phase contrast and the X-ray beam used was not monochromatic but had a wide energy bandwidth; however, two types of voids were accurately observed: one surrounded by a low-density rubber layer and the other with no such rubber layer. Voids surrounded by a low-density rubber layer tended to

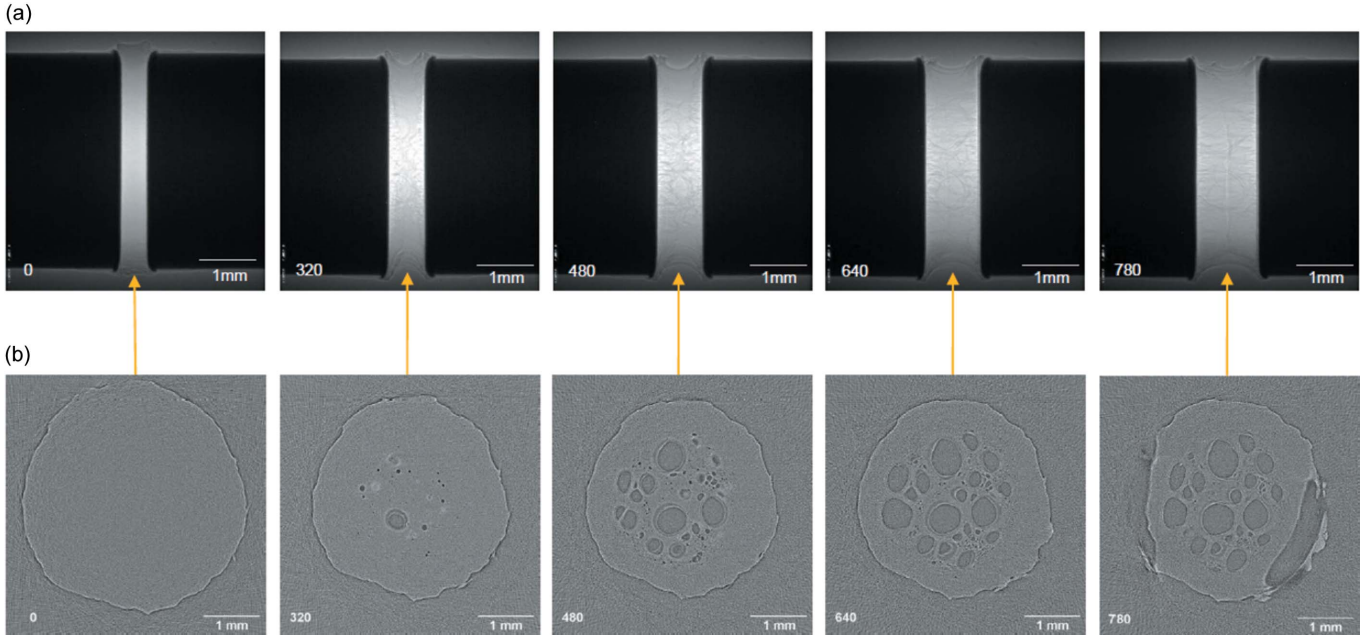

Figure 3
Time-resolved images of the tensile loading of rubber. The number in the bottom-left corner is the time in milliseconds from the beginning of elongation. (*a*) X-ray projection images at the mentioned time. (*b*) X-ray tomograms of the middle of the top of the two rods.

grow to larger sizes, indicating the existence of parts where voids grow more easily within the rubber due to its heterogeneity. Therefore, preventing the formation of voids with a low-density rubber layer is critical for improving the fracture resistance property of rubber. The fracture mechanism of rubber has not been elucidated because of the complexity of the fracture phenomenon, such as polymer chain relaxation and stress concentration due to the heterogeneous structure of the materials in rubber (Kishimoto *et al.*, 2008; Ishikawa & Chiba, 1990; Uesugi *et al.*, 2016). Detailed analysis of the fracture phenomenon with the high temporal resolution of this method assists in the complete elucidation of the fracture mechanism of rubber.

4. Discussion

One of the benefits and unique capabilities of our equipment is that it can be applied to observe even unspontaneous and unrepeatable phenomena. An application of our equipment with the highest social need is the real-time observation of soft-material fractures under external loads, as elucidated in this paper. For example, in the case of rubber materials for tires, X-ray CT observation of the breaking process of rubber with high temporal resolution such as that presented in our study has not been previously reported. If the unexplained fracture phenomenon of rubber is revealed and the fracture resistance property of tire rubber can be improved because of this unprecedented technique, a solution for a social issue such as the conservation of a natural resource like rubber can be found.

Large field of view (FOV) and high spatial resolution are the other benefits of our equipment. As a white synchrotron X-ray beam from a bending magnet or a wiggler generally has very high flux and centimetre-order size, it enables the realization of a large FOV (5 mm × 5 mm) as well as high spatial resolution (5 µm). One of the limitations of our equipment is its high rotation speed, which can deform a soft sample or kill an insect. In the case of the rubber sample used in this study, X-ray tomography at rotation speeds higher than 6000 rpm was difficult because of the centrifugal force acting on the sample. Hence, multibeam X-ray imaging systems, reported in previous papers (Hoshino *et al.*, 2011, 2013; Villanueva-Perez *et al.*, 2018; Voegeli *et al.*, 2020) are required for temporal resolutions higher than 5 ms. Although the number of projections is limited in such multibeam X-ray imaging systems, state-of-the-art data science techniques, such as the compressed sensing algorithms described in Section 3, enable the realization of millisecond-order X-ray tomography from tens of projections. In contrast, the X-ray imaging system presented in this study can provide a large FOV and a large number of projection images, leading to high spatial resolution, even when the conventional tomographic reconstruction algorithm is used. This can be advantageous for relatively hard and small materials, which exhibit negligible distortion due to centrifugal force.

For scientific applications, quantitative tomographic reconstruction is often desired. As the tomograms shown in Fig. 3(*b*) and Movie S1 are reconstructed from images including propagation-based phase contrast due to a white X-ray beam with high spatial coherence, they are not quantitative. Quantitative tomographic reconstruction from such propagation-based phase-contrast images requires the so-called quasihomogeneous assumption (García-Moreno *et al.*, 2019; Paganin *et al.*, 2002; Bronnikov, 2002; Chen *et al.*, 2013; Groso *et al.*, 2006; Walker *et al.*, 2014; Xu *et al.*, 2016; Ruhlandt *et al.*, 2017), which is not generally satisfied. Without this special assumption, grating-based X-ray interferometry (David *et al.*, 2002; Momose *et al.*, 2003; Weitkamp *et al.*, 2005; Pfeiffer *et al.*, 2006, 2008; Yashiro *et al.*, 2010, 2019; Yashiro, 2018) allows quantitative tomographic reconstruction. Although its sensitivity is lower than that of X-ray crystal interferometry (Yoneyama *et al.*, 2006, 2018; Takeda *et al.*, 2012), it has the advantage of using a white synchrotron X-ray beam. Recently, we demonstrated that the application of a fringe scan can improve the spatial resolution and signal-to-noise ratio of the tomograms obtained in grating-based X-ray interferometry, and successfully realized quantitative X-ray phase tomography for a rotating sample with millisecond-order measurement time (Yashiro *et al.*, 2018*a*). A higher temporal resolution can be realized with a higher sample rotation speed, if an X-ray source with higher-brilliance, such as an undulator or an X-ray free-electron laser, is used (Rack *et al.*, 2014; Olbinado *et al.*, 2017, 2018; Escauriza *et al.*, 2018; Vagovič *et al.*, 2019). However, their beam sizes are of millimetre-order, limiting their FOVs, and the higher rotation speed further limits their application.

Funding information

The following funding is acknowledged: JST CREST (grant No. JPMJCR1765). The X-ray tomography experiments were performed at BL28B2 of SPring-8 with the approval of the Japan Synchrotron Radiation Research Institute (JASRI) (proposal Nos. 2017A1202, 2017B1406 and 2019B1593).

References

Bronnikov, A. V. (2002). *J. Opt. Soc. Am. A*, **19**, 472–480.
Bruning, J. H., Herriott, D. R., Gallagher, J. E., Rosenfeld, D. P., White, A. D. & Brangaccio, D. J. (1974). *Appl. Opt.* **13**, 2693–2703.
Chen, R. C., Rigon, L. & Longo, R. (2013). *Opt. Express*, **21**, 7384–7399.
Cloetens, P., Barrett, R., Baruchel, J., Guigay, J.-P. & Schlenker, M. (1996). *J. Phys. D Appl. Phys.* **29**, 133–146.
David, C., Nöhammer, B., Solak, H. H. & Ziegler, E. (2002). *Appl. Phys. Lett.* **81**, 3287–3289.
Defrise, M., Vanhove, C. & Liu, X. (2011). *Inverse Probl.* **27**, 065002.
Donoho, D. L. (2006). *IEEE Trans. Inf. Theory*, **52**, 1289–1306.
Escauriza, E. M., Olbinado, M. P., Rutherford, M. E., Chapman, D. J., Jonsson, J. C. Z., Rack, A. & Eakins, D. E. (2018). *Appl. Opt.* **57**, 5004–5010.
García-Moreno, F., Kamm, P. H., Neu, T. R., Bülk, F., Mokso, R., Schlepütz, C. M., Stampanoni, M. & Banhart, J. (2019). *Nat. Commun.* **10**, 3762.
Groso, A., Abela, R. & Stampanoni, M. (2006). *Opt. Express*, **14**, 8103–8110.
Hack, E. & Burke, J. (2011). *Rev. Sci. Instrum.* **82**, 061101.

Hoshino, M., Sera, T., Uesugi, K. & Yagi, N. (2013). *J. Instrum.* **8**, C05002.
Hoshino, M., Uesugi, K., Pearson, J., Sonobe, T., Shirai, M. & Yagi, N. (2011). *J. Synchrotron Rad.* **18**, 569–574.
Ishikawa, M. & Chiba, I. (1990). *Polymer*, **31**, 1232–1238.
Kamada, K., Endo, T., Tsutumi, K., Yanagida, T., Fujimoto, Y., Fukabori, A., Yoshikawa, A., Pejchal, J. & Nikl, M. (2011). *Cryst. Growth Des.* **11**, 4484–4490.
Kishimoto, H., Shinohara, Y., Amemiya, Y., Inoue, K., Suzuki, Y., Takeuchi, A., Uesugi, K. & Yagi, N. (2008). *Rubber Chem. Technol.* **81**, 541–551.
Kudo, H., Yamazaki, F., Nemoto, T. & Takaki, K. (2016). *Proc. SPIE*, **9967**, 996711.
Lee, J. S., Weon, B. M., Park, S. J., Je, J. H., Fezzaa, K. & Lee, W.-K. (2011). *Nat. Commun.* **2**, 367.
Li, M. H., Yang, H. Q. & Kudo, H. (2002). *Phys. Med. Biol.* **47**, 2599–2609.
Momose, A., Kawamoto, S., Koyama, L., Hamaishi, Y., Takai, K. & Suzuki, Y. (2003). *Jpn. J. Appl. Phys.* **42**, L866–L868.
Olbinado, M. P., Grenzer, J., Pradel, P., Resseguier, T. D., Vagovic, P., Zdora, M.-C., Guzenko, V. A., David, C. & Rack, A. (2018). *J. Instrum.* **13**, C04004.
Olbinado, M. P., Just, X., Gelet, J.-L., Lhuissier, P., Scheel, M., Vagovič, P., Sato, T., Graceffa, R., Schulz, J., Mancuso, A., Morse, J. & Rack, A. (2017). *Opt. Express*, **25**, 13857–13871.
Paganin, D., Mayo, S. C., Gureyev, T. E., Miller, P. R. & Wilkins, S. W. (2002). *J. Microsc.* **206**, 33–40.
Pfeiffer, F., Bech, M., Bunk, O., Kraft, P., Eikenberry, E. F., Brönnimann, Ch., Grünzweig, C. & David, C. (2008). *Nat. Mater.* **7**, 134–137.
Pfeiffer, F., Weitkamp, T., Bunk, O. & David, C. (2006). *Nat. Phys.* **2**, 258–261.
Rack, A., Scheel, M., Hardy, L., Curfs, C., Bonnin, A. & Reichert, H. (2014). *J. Synchrotron Rad.* **21**, 815–818.
Ruhlandt, A., Töpperwien, M., Krenkel, M., Mokso, R. & Salditt, T. (2017). *Sci. Rep.* **7**, 6487.
Schreiber, H. & Bruning, J. H. (2007). *Optical Shop Testing*, 3rd ed., edited by D. Malacara, pp. 547–666. Hoboken, NJ: Wiley.
Sidky, E. Y. & Pan, X. (2008). *Phys. Med. Biol.* **53**, 4777–4807.
Snigirev, A., Snigireva, I., Kohn, V., Kuznetsov, S. & Schelokov, I. (1995). *Rev. Sci. Instrum.* **66**, 5486–5492.
Socha, J. J., Westneat, M. W., Harrison, J. F., Waters, J. S. & Lee, W.-K. (2007). *BMC Biol.* **5**, 6.
Takeda, T., Yoneyama, A., Wu, J., Lwin T.-T., Momose, A. & Hyodo, K. (2012). *J. Synchrotron Rad.* **19**, 252–256.
Uesugi, K., Hoshino, M., Kishimoto, H. & Mashita, R. (2016). *Proc. SPIE*, **9967**, 99670V.
Vagovič, P., Sato, T., Mikeš, L., Mills, G., Graceffa, R., Mattson, F., Villanueva-Perez, P., Ershov, A., Faragó, T., Uličný, J., Kirkwood, H., Letrun, R., Mokso, R., Zdora, M.-C., Olbinado, M. P., Rack, A., Baumbach, T., Schulz, J., Meents, A., Chapman, H. N. & Mancuso, A. P. (2019). *Optica*, **6**, 1106–1109.
Villanueva-Perez, P., Pedrini, B., Mokso, R., Vagovic, P., Guzenko, V. A., Leake, S. J., Willmott, P. R., Oberta, P., David, C., Chapman, H. N. & Stampanoni, M. (2018). *Optica*, **5**, 1521–1524.
Voegeli, W., Kajiwara, K., Kudo, H., Shirasawa, T., Liang, X. & Yashiro, W. (2020). *Optica*, **7**, 514–517.
Walker, S. M., Schwyn, D. A., Mokso, R., Wicklein, M., Müller, T., Doube, M., Stampanoni, M., Krapp, H. G. & Taylor, G. K. (2014). *PLoS Biol.* **12**, e1001823.
Wang, T., Kudo, H., Yamazaki, F. & Liu, H. (2019). *Phys. Med. Biol.* **64**, 145006.
Weitkamp, T., Diaz, A., David, C., Pfeiffer, F., Stampanoni, M., Cloetens, P. & Ziegler, E. (2005). *Opt. Express*, **13**, 6296–6304.
Wilkins, S. W., Gureyev, T. E., Gao, D., Pogany, A. & Stevenson, A. W. (1996). *Nature*, **384**, 335–338.
Xu, L., Chen, R. C., Du, G. H., Yang, Y. M., Wang, F. X., Deng, B. A., Xie, H. L. & Xiao, T. Q. (2016). *Sci. Rep.* **6**, 32380.
Yashiro, W. (2018). *Microscopy*, **67**, 303–316.
Yashiro, W., Ikeda, S., Wada, Y., Totsu, K., Suzuki, Y. & Takeuchi, A. (2019). *Sci. Rep.* **9**, 14120.
Yashiro, W., Kamezawa, C., Noda, D. & Kajiwara, K. (2018*a*). *Appl. Phys. Expr.* **11**, 122501.
Yashiro, W., Noda, D. & Kajiwara, K. (2017*a*). *Appl. Phys. Expr.* **10**, 052501.
Yashiro, W., Noda, D. & Kajiwara, K. (2018*b*). *Opt. Express*, **26**, 1012–1027.
Yashiro, W., Terui, Y., Kawabata, K. & Momose, A. (2010). *Opt. Express*, **18**, 16890–16891.
Yashiro, W., Ueda, R., Kajiwara, K., Noda, D. & Kudo, H. (2017*b*). *Jpn. J. Appl. Phys.* **56**, 112503.
Yoneyama, A., Amino, N., Mori, M., Kudoh, M., Takeda, T., Hyodo, K. & Hirai, Y. (2006). *Jpn. J. Appl. Phys.* **45**, 1864–1868.
Yoneyama, A., Iizuka, A., Fujii, T., Hyodo, K. & Hayakawa, J. (2018). *Sci. Rep.* **8**, 12674.